A Statistical Model of Retinal Optical Coherence Tomography Image Data

Prathamesh Kulkarni, Diana Lozano, George Zouridakis, and Michael Twa

Abstract—**Optical coherence tomography (OCT) is an important mode of biomedical imaging for the diagnosis and management of ocular disease. Here we report on the construction of a synthetic retinal OCT image data set that may be used for quantitative analysis of image processing methods. Synthetic image data were generated from statistical characteristics of real images (n = 14). Features include: multiple stratified layers with representative thickness, boundary gradients, contour, and intensity distributions derived from real data. The synthetic data also include retinal vasculature with typical signal obscuration beneath vessels. This synthetic retinal image can provide a realistic simulated data set to help quantify the performance of image processing algorithms.**

I. INTRODUCTION

OPTICAL coherence tomography (OCT) imaging of the eye has rapidly become one of the most important imaging modalities for the diagnosis and management of retinal diseases. Current state of the art Spectral Domain OCT (SD-OCT) imaging systems provide clinicians with micron-level resolution [1-3]. This technology has moved rapidly from engineering to clinical implementation and tools to quantify and assist users with visualization and interpretation of the data generated are still developing [4-7].

Quantitative analysis of biomedical image data plays an increasingly important role in medical decision making. Feature detection may be an important component of tumor identification in breast cancer [8-13] and image segmentation may be critical information that helps clinicians to decide whether or not medical therapy is halting the progression of optic nerve degeneration in glaucoma [14, 15]. Biomedical image information is also increasingly used as guidance for surgical treatments [16]. Each of these applications relies on various elements of image processing that may include feature detection, segmentation, registration, and denoising as well as other operations. Reliable quantitative analysis of image data is an important step in deriving actionable information from imaging data.

There are numerous studies that use synthetic or phantom images as a benchmark to enable quantitative comparisons of image processing operations. For example, the modified Shepp-Logan phantom is frequently used as a reference for CT and MRI image processing evaluations. Despite its simplicity (or perhaps because of it) this model has been a highly useful tool for quantitative analysis of image processing methods in MRI and CT data [17, 18]. Phantom images have also been used for validation of image registration [20] and segmentation algorithms [21, 22] for ultrasound data. However, these synthetic images were not derived from real data. In this research, we derive a synthetic model for retinal OCT data from real image data. The objective of this research was to develop a model of retinal SD-OCT data that could be used as a benchmark for similar quantitative research with OCT image data. The goal was to provide a standardized synthetic data set for comparison of various image processing methods.

II. METHODS

A. Data

Fourteen high-quality B-Scan images were selected from within three different C-Scan volumes, each from a different animal. All parameters of the model were derived using these fourteen images. To insure that all B-Scan images had comparable thickness parameters for each layer, the B-Scan images were selected from regions adjacent to the optic nerve head (**Figure 1**).

B. Manual segmentation

Each B-Scan image included in the model was manually segmented by domain experts using a custom designed image annotation tool. The segmentation procedure involved delineating the boundaries for seven different retinal layers and demarcating blood vessels in the image. The seven layers included in the segmentations were: Nerve Fiber Layer-Ganglion Cell Layer (NFL-GCL), Inner Plexiform Layer (IPL), Inner Nuclear Layer (INL), Outer Plexiform Layer (OPL), Outer Nuclear Layer (ONL), Photo Receptor Layer (PRL) and Retinal Pigmented Epithelium (RPE). Each of these layers is identified separately in **Figure 2**. Manual segmentation of these multiple images was the basis for the intensity, gradient and contour parameters of the synthetic image model.

C. Intensity modeling

Intensity distribution models were derived for seven retinal layers by analyzing the distributions for these layers across

the fourteen constituent B-Scan images. Statistical analysis was performed to evaluate the intensity distributions to determine whether or not they were normal, kurtotic, or showed any significant skew. The Shapiro-Francia test for normality was used to evaluate each distribution (Stata x86-64 v11.2). **Table 1** shows the results for the Shapiro-Francia
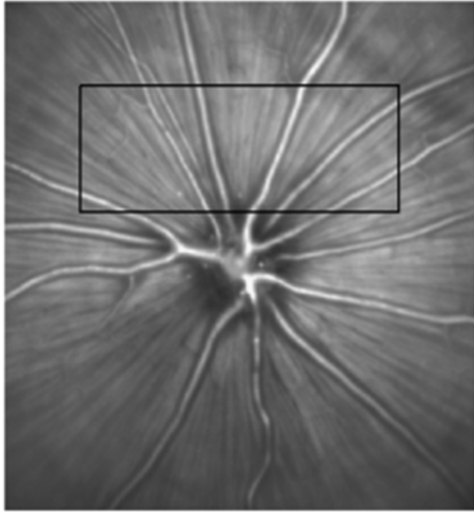

Figure 1. Scanning laser retinal image. Box indicates the relative location where the OCT data was acquired 1-2 mm away from the optic nerve head center.

test for normality applied to the distributions of each layer from the fourteen B-Scan images, with $P < .05$ indicating a statistically significant departure from normality. Statistical test results as well as graphical inspection were the basis for selection of the modeled probability distributions. Layers modeled with Normal distributions had their respective means and standard deviations derived from the mean of the 14 total B-Scan images. The remaining layers that were significantly different from standard Normal probability distributions were modeled as Generalized Extreme Value (GEV) distributions. The corresponding with mean, standard deviation and a shape parameters were again derived from the 14 individual B-Scan images. The common feature observed among distributions that did not pass statistical tests for normality was that each had a right-skewed distribution. The shape parameter of the GEV distribution determines the amount and direction of skew present in the distributions. The equation for the GEV distribution with mean (μ), standard deviation (σ) and shape parameter ($k \neq 0$) is given by [19],

$$y = f(x|k, \mu, \sigma) = \left(\frac{1}{\sigma}\right) \exp\left(-\left(1 + \frac{k(x - \mu)}{\sigma}\right)^{-\frac{1}{k}}\right)\left(1 + \frac{k(x - \mu)}{\sigma}\right)^{-1-\frac{1}{k}} for\ 1 + \frac{k(x - \mu)}{\sigma} > 0.$$

Typical examples of Normal and GEV distributions that contributed to the model are shown in **Figure 4**. The parameters for each selected model are an average of the parameters contributed by each individual B-Scan image.

For example the mean intensity for the normal model of the IPL is the global mean of IPL across the fourteen constituent B-Scan images. These parameters (mean, standard deviation, and shape parameter) are shown in the last column of **Table 1**.

TABLE I
MODEL DESCRIPTION BY RETINAL LAYER

Layer name	Pass ratio	Model used	Parameters
NFL-GCL	4/14	Normal	(138.18, 33.48)
IPL	10/14	Normal	(92.48, 14.16)
INL	0/14	GEV	(53.47, 7.87, -0.09)
OPL	0/14	GEV	(92.48, 14.05, -0.12)
ONL	5/14	Normal	(53.47, 7.87)
PRL	6/14	GEV	(111.72, 17.37, -0.15)
RPE	2/14	Normal	(115.36, 24.19)

Pass ratio: number of images which passed the Shapiro-Francia normality test (number passed/total number of images). Two types of models were used to model the retinal layer intensity distributions: Normal and Generalized Extreme Value (GEV) distributions. Parameters: mean, standard deviation, shape parameter (only for GEV). Nerve Fiber Layer-Ganglion Cell Layer (NFL-GCL), Inner Plexiform Layer (IPL), Inner Nuclear Layer (INL), Outer Plexiform Layer (OPL), Outer Nuclear Layer (ONL), Photo Receptor Layer (PRL), Retinal Pigment Epithelium (RPE).

D. Contour and gradient modeling

Average contours were derived from the manually segmented B-Scan images belonging to the same C-Scan image. This gives an estimate of the average location and thickness of each layer for that C-Scan.

The average gradient profile is calculated from the non-vascular region of the B-Scan images belonging to the a particular C-Scan. This gradient profile was then used as a multiplicative model to represent the real gradient in the synthetic images.

E. Blood vessel modeling

Sample blood vessels were extracted from the B-Scan images. A blood vessel template representing the approximate structure and intensity of the blood vessels was constructed from these extracted structural templates. Such templates were then manually added to the vascular regions of the synthetic images. To simulate the blood vessel shadows found in real images, the regions underneath the blood vessels were multiplied by a scalar resulting in an overall shift in the layer distributions under the blood vessels.

F. Global noise modeling

Speckle noise is inherently present in OCT images. In order to model this phenomenon, global speckle noise of varying standard deviations was added to the synthetic image. This model parameter can be used to vary the overall quality of the synthetic images. This can be useful in testing the performance of segmentation and denoising algorithms on OCT data in the presence of noise variations.

III. RESULTS

Synthetic images were created using the above described model. **Figure 2** shows a sample B-Scan image from among those contributing to the model. The corresponding
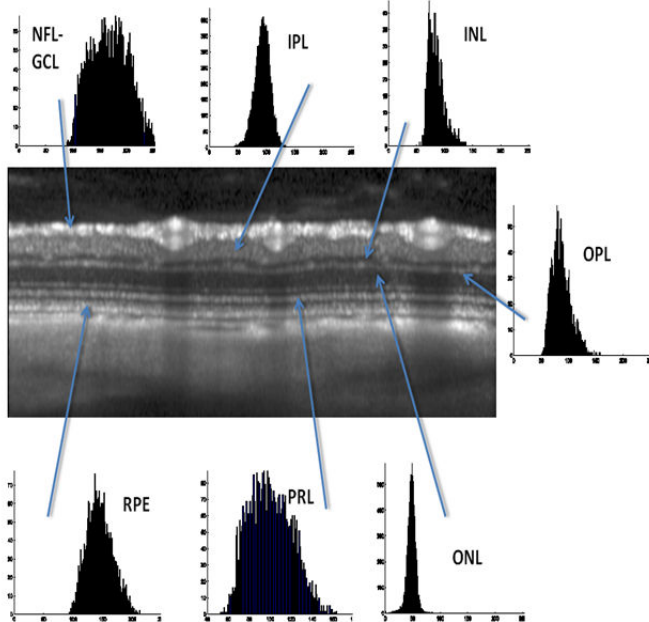

Figure 2. Real OCT B-Scan image with arrows pointing to the individual retinal layers and thumbnails showing the corresponding intensity distributions.

distributions of the layers within this image are also identified. **Figure 2** is a typical OCT B-Scan image demonstrating the different stratified layers of the neural retina. The topmost layer (Nerve Fiber Layer-Ganglion Cell Layer) is the brightest among all the layers with prominent circularly shaped blood vessels. There are 3 large vessels seen casting prominent shadows beneath their blood column in **Figure 1**. An hour-glass structural formation is seen within the blood vessel lumen formed by the intensity variations that is characteristic of retinal blood vessels imaged by OCT. The second relatively darker and thicker layer is the Inner Plexiform Layer. Below this layer is a thin dark band: the Inner Nuclear Layer. This is followed by the similarly thin, but brighter Outer Plexiform Layer. Below that is the thick, prominent, and dark Outer Nuclear layer which is similar in intensity to the inner nuclear layer.

The photoreceptor layer is beneath the outer nuclear layer and is seen as an intermittent banded layer. The photoreceptor layer is comprised of the inner and outer segments of these cells, each of which contributes to a different intensity and structure to make the irregularly banded appearance of this layer. Due to the lack of reliable and distinct structure in this layer we modeled these cells a single layer. The final layer included in our model is the Retinal Pigmented Epithelium. This is a relatively bright narrow layer adjacent to the deep vascular layer (choroid) and external outer tunic of the eye (sclera). Neither the choroid nor the sclera are part of the neural retina and are

not modeled here.

By inspection of the intensity distributions by layer, most of the layers could be modeled using either a normal or right-skewed distribution. Also, the two nuclear and plexiform layers have relatively similar intensity
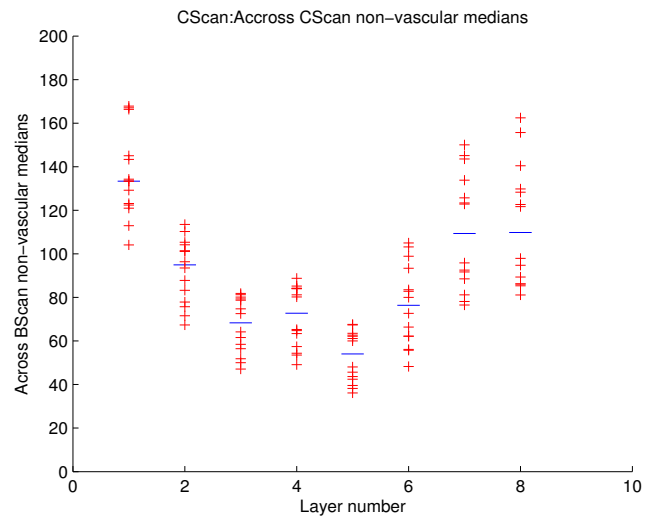

Figure 3. Distribution of median pixel intensity by layer across fourteen different B-Scan images that contributed to the model.
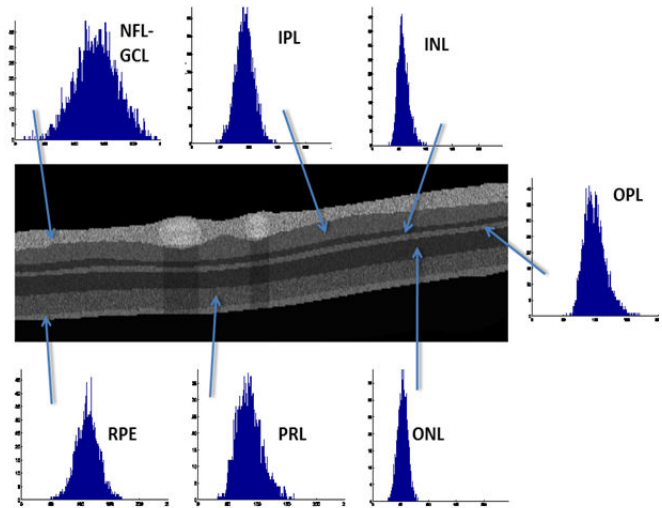

Figure 4. Synthetic B-Scan image with arrows pointing to individual synthesized retinal layers and thumbnails showing the corresponding intensity distributions. The blood vessels and their artifacts can also be observed here.

distributions that permitted us to use similar models for each of these respective layers.

Figure 3 shows the layer-wise variation of median intensity across all the fourteen constituent B-Scan images. The overall variation in intensity across layers described above is demonstrated in this figure. It can be observed that almost all the layers have compact distributions with no significant skew. This distribution across multiple B-Scan images and across multiple C-Scan volumes provides a rationale for selecting the global intensity parameters of a layer as the average over the parameters of that layer derived from the 14 B-Scan images.

Figure 4 shows a synthetic image and the intensity distributions modeled for each of the layers. The contours of the layers of the synthetic image represent the average of contours manually annotated from four B-Scan images. Every pixel within a layer of the synthetic image is randomly drawn from the corresponding modeled intensity distribution function for that layer. After the contour and intensity parameters were applied to the synthetic data array, the gradient model is then multiplied to this synthetic image. Simulated blood vessel templates are then added to the vascular region of the retinal nerve fiber layer. Lastly, shadows are added beneath the added vessels in order to model the reduced intensity and contrast seen beneath blood vessels in the real OCT images. The agreement of the model distributions by layer can be compared with a sample of real data by comparing the distributions in **Figures 2 and 4**.

IV. DISCUSSION

In this research we describe the basis and development of a statistical model of retinal OCT image data from manual segmentation of real data. This model characterizes many of the most relevant features present in real data including: intensity, contour, gradient, blood vessels, blood vessel artifacts and global noise derived from real OCT image data. While our use of manual segmentation as the basis for model parameters may be a limitation of this preliminary study, selection of an appropriate gold-standard is not a trivial problem. Despite this potential limitation, our proposed model provides a useful tool for future studies. First, it provides a test bed for quantifying the effects of various image processing routines such as, denoising, registration and segmentation. Moreover, it will provide us with a stable benchmark to evaluate the statistical performance of these operations. Imaging performance and anatomical structure can vary in both healthy and in pathological eyes due to many factors, including some that relate to pathological conditions under study. This model can provide a flexible test-bed easily adapted for these varying conditions.

Further development of this synthetic image data will permit us to simulate and assess the experimental effects of varying imaging conditions such as cataract, detector noise, or other parameters. Future improvements in this synthetic model should include additional parameters such as consideration for lateral and axial resolution as well as global retinal curvature which are not currently being modeled. Moreover, it would be easy and useful to apply a similar kind of modeling strategy for other types of retinal data (ex. human retinal OCT data) and also other imaging modalities (ex. ultrasound). Finally, this concept can be easily extended to create 3-D synthetic data to assess volumetric image processing methods.

REFERENCES

[1] M. F. Cordeiro, *et al.*, "High-resolution ocular imaging: combining advanced optics and microtechnology," *Ophthalmic Surg Lasers Imaging,* vol. 40, pp. 480-8, Sep-Oct 2009.

[2] B. Povazay, *et al.*, "Impact of enhanced resolution, speed and penetration on three-dimensional retinal optical coherence tomography," *Opt Express,* vol. 17, pp. 4134-50, Mar 2 2009.

[3] A. J. Witkin, *et al.*, "Ultra-high resolution optical coherence tomography assessment of photoreceptors in retinitis pigmentosa and related diseases," *Am J Ophthalmol,* vol. 142, pp. 945-52, Dec 2006.

[4] E. M. Anger, *et al.*, "Ultrahigh resolution optical coherence tomography of the monkey fovea. Identification of retinal sublayers by correlation with semithin histology sections," *Exp Eye Res,* vol. 78, pp. 1117-25, Jun 2004.

[5] R. Bernardes, *et al.*, "Improved adaptive complex diffusion despeckling filter," *Optics Express,* vol. 18, pp. 24048-24059, 2010.

[6] H. M. Salinas and D. C. Fernandez, "Comparison of PDE-Based Nonlinear Diffusion Approaches for Image Enhancement and Denoising in Optical Coherence Tomography," *Medical Imaging, IEEE Transactions on,* vol. 26, pp. 761-771, 2007.

[7] M. Gloesmann, *et al.*, "Histologic correlation of pig retina radial stratification with ultrahigh-resolution optical coherence tomography," *Invest Ophthalmol Vis Sci,* vol. 44, pp. 1696-703, Apr 2003.

[8] H. P. Chan, "Computer-aided diagnosis in breast tomosynthesis and chest CT," *Nippon Hoshasen Gijutsu Gakkai Zasshi,* vol. 65, pp. 968-76, Jul 20 2009.

[9] S. Fantini, *et al.*, "Spatial and spectral information in optical mammography," *Technol Cancer Res Treat,* vol. 4, pp. 471-82, Oct 2005.

[10] J. C. Fu, *et al.*, "Image segmentation feature selection and pattern classification for mammographic microcalcifications," *Comput Med Imaging Graph,* vol. 29, pp. 419-29, Sep 2005.

[11] G. Kim, *et al.*, "Indocyanine-green-embedded PEBBLEs as a contrast agent for photoacoustic imaging," *J Biomed Opt,* vol. 12, p. 044020, Jul-Aug 2007.

[12] A. Penn, *et al.*, "Morphologic blooming in breast MRI as a characterization of margin for discriminating benign from malignant lesions," *Acad Radiol,* vol. 13, pp. 1344-54, Nov 2006.

[13] P. S. Rodrigues, *et al.*, "A new methodology based on q-entropy for breast lesion classification in 3-D ultrasound images," *Conf Proc IEEE Eng Med Biol Soc,* vol. 1, pp. 1048-51, 2006.

[14] Z. Burgansky-Eliash, *et al.*, "Optical coherence tomography machine learning classifiers for glaucoma detection: a preliminary study," *Invest Ophthalmol Vis Sci,* vol. 46, pp. 4147-52, Nov 2005.

[15] G. Wollstein, *et al.*, "Optical coherence tomography longitudinal evaluation of retinal nerve fiber layer thickness in glaucoma," *Arch Ophthalmol,* vol. 123, pp. 464-70, Apr 2005.

[16] H. Sano, *et al.*, "A case of sphenoid sinus meningoencephalocele repaired by an image-guided endoscopic endonasal approach," *Auris Nasus Larynx,* Mar 8 2011.

[17] A. Loukiala, *et al.*, "Gap-filling methods for 3D PlanTIS data," *Phys Med Biol,* vol. 55, pp. 6125-39, Oct 21 2010.

[18] Z. Cao, *et al.*, "Optimal number of views in 360 degrees SPECT imaging," *J Nucl Med,* vol. 37, pp. 1740-4, Oct 1996.

[19] Kotz S and Nadarajah S, "Extreme Value Distributions: Theory and Applications", *Imperial College Press*, 2000.

[20] `Sanches J and Marques J, "Joint Image Registration and Volume Reconstruction for 3D Ultrasound." *Pattern Recognition Letters*, vol. 24, pp. 791-800, 2003.

[21] Xiao G, *et al.*, "Segmentation of Ultrasound B-Mode Images with Intensity Inhomogeneity Correction," *IEEE Transactions on Medical Imaging*, vol. 21, pp. 48-57, 2002.

[22] Boukerroui D, *et al.*, "Segmentation of Ultrasound Images - Multiresolution 2D and 3D Algorithm based on Global and Local Statistics," *Pattern Recognition Letters*, vol. 24, pp. 779-90, 2003.